Delft University of Technology

Polyacrylamide-Poly(vinyl alcohol)-Sodium Alginate-Reduced Graphene Oxide/Nylon Fabrics with Multistimuli Responses

Chen, Yuanyuan; Dai, Hanqing; Yan, Yukun; Piao, Zhiyan; Lu, Hanxu; Hu, Zhe; Wei, Wei; Zhang, Guoqi; Zhang, Wanlu; Guo, Ruiqian

Important note
To cite this publication, please use the final published version (if applicable).
Please check the document version above.

Polyacrylamide–Poly(vinyl alcohol)–Sodium Alginate–Reduced Graphene Oxide/Nylon Fabrics with Multistimuli Responses

Yuanyuan Chen, Hanqing Dai,* Yukun Yan, Zhiyan Piao, Hanxu Lu, Zhe Hu, Wei Wei,* Guoqi Zhang,* Wanlu Zhang,* and Ruiqian Guo*

Read Online

ACCESS | Metrics & More | Article Recommendations | Supporting Information

ABSTRACT: In recent years, various functional fabrics capable of responding to multistimuli have been widely recognized as promising wearable devices. However, the obtained composite functional fabrics have only been applied in a few scenarios, rendering the achievement of multifunctional wearable application scenarios a difficult goal. Therefore, there is an urgent need to expand the diversity of wearable applications for functional fabrics. Herein, we design hydrogel composite fabrics capable of responding to multiple stimuli, including vibration, temperature, strain, and pressure, to enable wearable multiapplication scenarios. The hydrogel composite fabrics, based on nylon fabrics (NFs), are fabricated with polyacrylamide (PAM)−poly(vinyl alcohol) (PVA)−sodium alginate (SA)−reduced graphene oxide (rGO)/NFs (PAM−PVA−SA−rGO/NFs). The PAM−PVA−SA−rGO/NFs exhibit a higher elastic stiffness coefficient (2.79 N cm^{-1}) than the blank NFs (1.76 N cm^{-1}), good temperature sensitivity in the range of 30−80 °C, and excellent detecting ability for urine presence with a threshold of unit area of 2.55×10^{-3} mL cm^{-2}. The PAM−PVA−SA−rGO/NFs can not only respond to multiple stimuli but also be integrated into clothing for wearable multiapplication scenarios, such as detecting human speaking and breathing, intelligent sleeves, and diaper alarms. Additionally, the mechanisms of the above phenomena are revealed. These results indicate that the PAM−PVA−SA−rGO/NFs will provide inspiration for the development of intelligence systems, feedback devices, soft robotics, wearable devices, etc.

KEYWORDS: *multistimuli responses, hydrogel composite fabrics, intelligent sleeves, intelligent diaper alarms, wearable multiapplication scenarios*
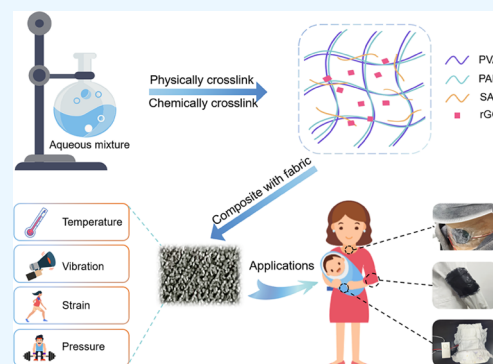
1. INTRODUCTION

Wearable devices allow for real-time monitoring of an individual's health status over an extended period through long-term and efficient services.[1−5] In particular, motion tracking can be utilized to analyze daily activities, such as joint motion monitoring, rehabilitation training, and chronic disease diagnosis.[6−9] The integration of humidity and temperature sensors into wearable devices allows for the detection of human urine, respiration, sweat, and temperature information.[10−12] Moreover, the fabrics covering our body surface receive a large amount of data from the human body, including sound, light, electricity, and biological signals, which is the most ideal application scenario for wearable devices. When wearable devices can be seamlessly integrated into clothing, such as hats, shirts, and socks, with minimal impact on comfort and lightweight, these functional fabrics can effectively detect various vital signs, including tension, pressure, temperature, breathing, and voice. And further, these fabrics can realize the functions of storage, analysis, inference, and reminder.

Meeting these aforementioned requirements often requires the combination of fabrics with various materials possessing distinct properties. Recently, conductive materials have been used to compound with fabrics to realize various sensing functions, and the conductive materials reported include metals and their derivatives,[13,14] conductive polymers,[15,16] liquid electrodes,[17] and so on. Among these materials, conductive hydrogels have been most commonly used because of their superior biocompatibility and comfort.[18,19] However, many of the existing functional fabrics have been found only responding to few stimuli or only suited to few wearable scenarios.[20−22] Therefore, this inability to simultaneously achieve multistimuli responses and diversified wearable application scenarios highlights a critical need to expand both multistimuli responses and multiapplication scenarios for these functional fabrics.
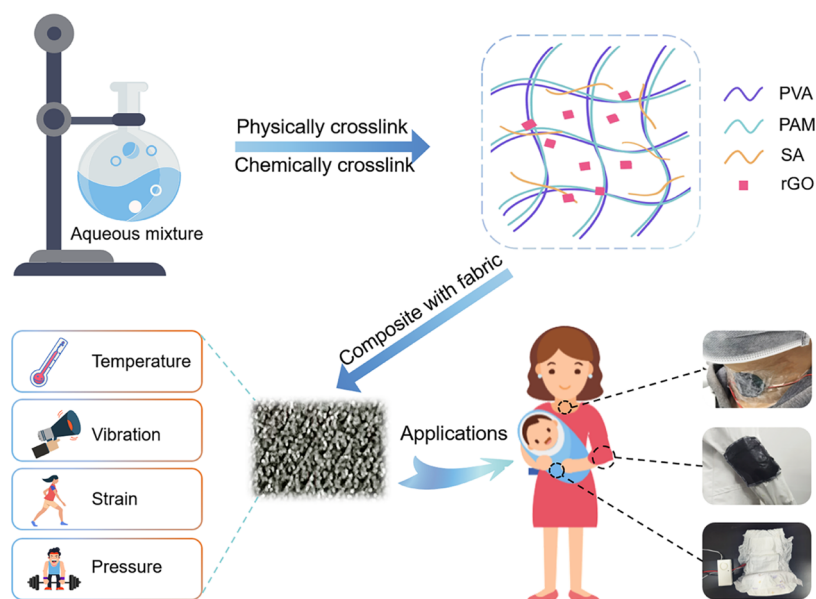
Figure 1. Materials synthesis, photographs, sensing properties, and applications of the PAM−PVA−SA−rGO/NFs. The PAM−PVA−SA−rGO quaternary hydrogel system was fabricated by a one-step free radical polymerization method with ultrasonic dispersion. In this hydrogel system, PAM−PVA−SA formed a triple interpenetrating network hydrogel, and rGO was dispersed into the hydrogel as a conductive filler. Then, the PAM−PVA−SA−rGO/NFs were fabricated by compounding the NFs with the PAM−PVA−SA−rGO hydrogels. The PAM−PVA−SA−rGO/NFs can sense temperature, vibration, strain, and pressure. As for the applications, the PAM−PVA−SA−rGO/NFs could be applied in monitoring human speaking and breathing behaviors, intelligent sleeves, and diaper alarms.

Herein, we designed hydrogel composite fabrics capable of responding to multiple stimuli, including vibration, temperature, strain, and pressure, and realized wearable multi-application scenarios. The hydrogel composite fabrics, polyacrylamide−poly(vinyl alcohol)−sodium alginate−reduced graphene oxide/nylon fabrics (PAM−PVA−SA−rGO/NFs), were fabricated with a PAM−PVA−SA−rGO quaternary hydrogel system and NFs. This quaternary hydrogel system featured a PAM−PVA−SA triple interpenetrating network and rGO as a conductive filler, and there were synergized interactions between rGO and PAM, PVA, and SA chains. Due to the above properties, the PAM−PVA−SA−rGO/NFs could not only sense multistimuli but also be applied in multiapplication scenarios, such as monitoring human speaking and breathing behaviors, intelligent sleeves, and diaper alarms. These results indicated that the PAM−PVA−SA−rGO/NFs possessed great potential in intelligence systems, feedback devices, soft robotics, wearable devices, etc.

2. RESULTS AND DISCUSSION

As shown in Figure 1, the PAM−PVA−SA−rGO/NFs were fabricated by compounding NFs with a PAM−PVA−SA−rGO quaternary hydrogel system prepared by a one-step free radical polymerization method with ultrasonic dispersion. In this system, PAM−PVA−SA formed a triple interpenetrating network hydrogel, while rGO was dispersed into the hydrogel as a conductive filler.[23] The PAM chain formed a covalent cross-linking network through monomer copolymerization, enhancing the toughness of the hydrogel. The SA chain contained a large number of hydrophilic groups that aided in locking in the internal moisture. Due to the existence of rGO, the PAM−PVA−SA−rGO system had excellent electrical properties. In the PAM−PVA−SA−rGO/NF, the thickness (L) was 0.5 mm, and the bulk resistance (R_b) was 7.61 KΩ

(Figure S1), and the electrode contacting area (S) was 1.25 cm². Thus, according to the following equation

$$\sigma = \frac{L}{R_b \cdot S} \tag{1}$$

where the ionic conductivity (σ) of the PAM−PVA−SA−rGO/NF at room temperature was 5.26×10^{-4} S/m. The unit surface resistance of the PAM−PVA−SA−rGO/NF with a size of 4×4 cm² was 6.25 KΩ cm⁻². The PAM−PVA−SA−rGO/NFs exhibited good wettability with a low water contact angle (WCA) of 43° (Figure S2), indicating the successful combination of the PAM−PVA−SA−rGO hydrogel and NFs. Clearly, many gaps among fibers of the NFs were filled with hydrogels, producing more compact structures after the NFs were compounded with the PAM−PVA−SA−rGO hydrogels from the image of scanning electron microscopy (SEM), as displayed in Figure S3a. These phenomena could contribute to solving the issue of low sensing accuracy caused by insufficient contact.

The Fourier transform infrared (FTIR) spectroscopy was employed to explore the functional groups in the PAM−PVA−SA−rGO/NFs, and the results are shown in Figure S3b. A series of characteristic bands at 1067, 1259, and 1340 cm⁻¹ were attributed to C−O−C, C−O of C−OH, and −OH of C−OH, respectively, and corresponded to rGO.[24] The bands at 1421 and 3243 cm⁻¹ were due to −COO⁻ and −OH, which corresponded to the characteristic bands of SA.[25] The peaks at 3325 and 3189 cm⁻¹ were from N−H stretching vibration and those at 1642 and 1605 cm⁻¹ were due to C═O stretching vibration, which corresponded to the characteristic peaks of PAM.[26] The appearances of the bands at 2920, 2900, and 1097 cm⁻¹ were attributed to the C−O stretching vibration, C−H stretching vibration, and CH₂ asymmetric stretching vibration, respectively, which corresponded to the characteristic bands of PVA.[26,27] Therefore, the above results of the FTIR spectra
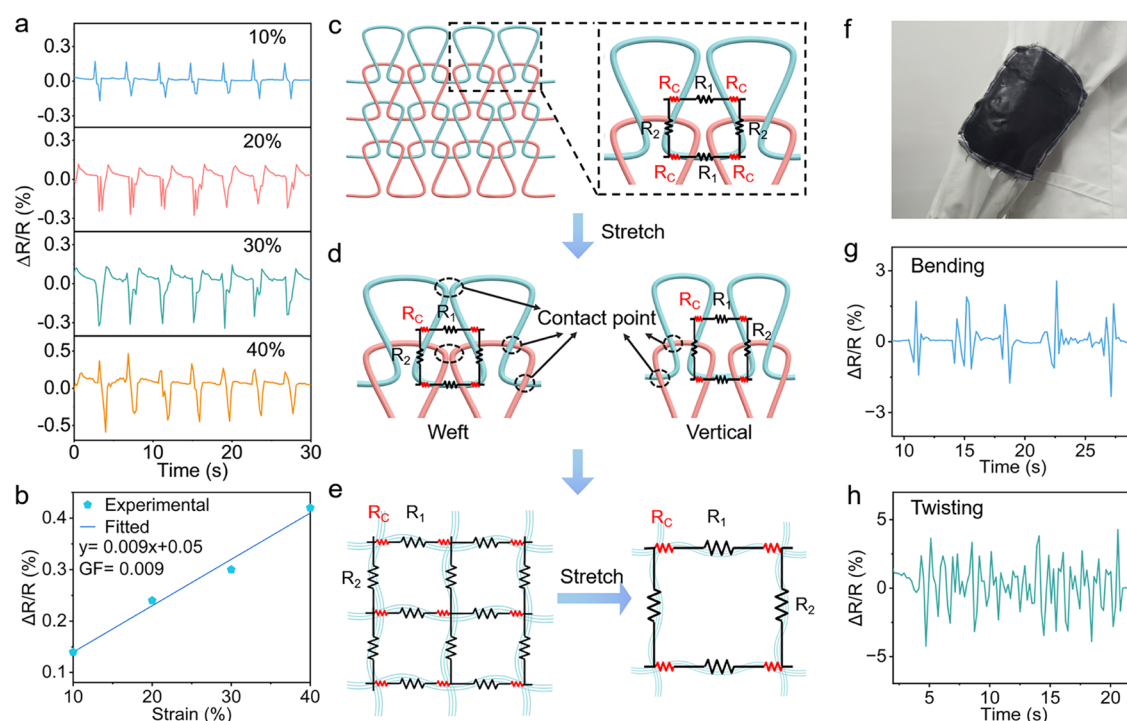
Figure 2. Strain sensing performances of the PAM−PVA−SA−rGO/NFs and application in intelligent sleeves. The relative changes of the resistance with different small tensile strain changes of 10−40% (a,b). (c) Schematic diagrams of a basic conductive unit of the conductive network in the PAM−PVA−SA−rGO/NFs. (d) Schematic diagrams of stretched knitted structures in the basic conductive unit of the PAM−PVA−SA−rGO/NFs. (e) Schematic diagrams of the simple models and equivalent circuits in the basic conductive unit of the PAM−PVA−SA−rGO/NFs. (f) Photo of the actual test of intelligent sleeves based on the PAM−PVA−SA−rGO/NFs. The relative changes of the resistance with bending (g) and twisting (h) movements of the intelligent sleeves.

confirmed the successful preparation of the PAM−PVA−SA−rGO/NFs.

In addition, the mechanical properties of PAM−PVA−SA−rGO/NFs were investigated. As shown in Figure S7, the PAM−PVA−SA−rGO hydrogel displayed a strain tolerance of 157.4% and stress of 35.8 kPa. The elastic stiffness coefficients of a piece of NF and a piece of PAM−PVA−SA−rGO/NF were 1.76 and 2.79 N cm^{-1}, respectively (Figure S3c), demonstrating that the incorporation of the PAM−PVA−SA−rGO hydrogel system enhanced the mechanical properties of the PAM−PVA−SA−rGO/NFs. The strong interaction between rGO and PAM, PVA, and SA chains, such as hydrogen bond, $\pi-\pi$ bond, and intermolecular interaction, functioned as a bridge to connect the network structure, thereby improving the mechanical properties of the system.[28,29] The triple interpenetrating network structure could effectively dissipate energy, further enhancing the mechanical strength of the PAM−PVA−SA−rGO system.[30] And meanwhile, the rheological properties of the PAM, PAM−PVA, PAM−PVA−SA, and PAM−PVA−SA−rGO composite hydrogels were also investigated (Figure S6), and the results indicated that the construction of interpenetrating triple networks enhanced the viscoelasticity of composite hydrogels. Besides, when the PAM−PVA−SA−rGO/NFs were rubbed and stuck with tape, there was no detachment of the PAM−PVA−SA−rGO hydrogels from the PAM−PVA−SA−rGO/NFs, indicating the impressive mechanical stability of the PAM−PVA−SA−rGO/NFs (Figure S3d,e). Compressing and stretching the hydrogels resulted in changes of the internal structure, and the stretching process led to an increase in resistance due to the increased network distances of the

hydrogels. Therefore, the PAM−PVA−SA−rGO/NFs based on the PAM−PVA−SA−rGO system held promise for multistimuli responsive sensing performances, such as strain, pressure, and vibration.

The strain sensing performances of the PAM−PVA−SA−rGO/NFs were investigated by the relative resistance change ($\Delta R/R$), as revealed in Figure 2. The results indicated that the PAM−PVA−SA−rGO/NFs showed excellent stability and repeatability in a tensile strain of 10−40% (Figure 2a). $\Delta R/R$ increased as the applied tensile strains increased (Figure 2b). $\Delta R/R$ to strain was linearly fitted by the equation $y = 0.009x + 0.05$. The slope of the fitted curve represented the gauge factor (GF) of the strain, and it was concluded that the GF of tensile strain in the range of 10−40% was approximately 0.009. Further analysis of the relative resistance changes was conducted to explore the mechanisms and resistance models (Figure 2c−e). Figure 2c shows a basic conductive unit of the conductive network of the PAM−PVA−SA−rGO/NFs in the initial state, and Figure 2d displays stretched knitted structures of the basic conductive unit. In the initial state, the PAM−PVA−SA−rGO hydrogels filled many gaps among fibers of the NFs, imparting conductivity to the PAM−PVA−SA−rGO/NFs. And in the weft-knitted structures, the contact points and conductive networks formed due to the amounts of contact among the PAM−PVA−SA−rGO hydrogels, ensuring the conductive pathways. When the tensile strain was applied, the conductive materials in the conductive network became dislocated or separated, and the contact points decreased.[31] As revealed in Figure 2c,d, a conductive unit could be divided into two parts ($R_2 + R_C + R_1 + R_C$ and $R_C + R_1 + R_C + R_2$) and regarded as a parallel circuit. Therefore, the total resistance
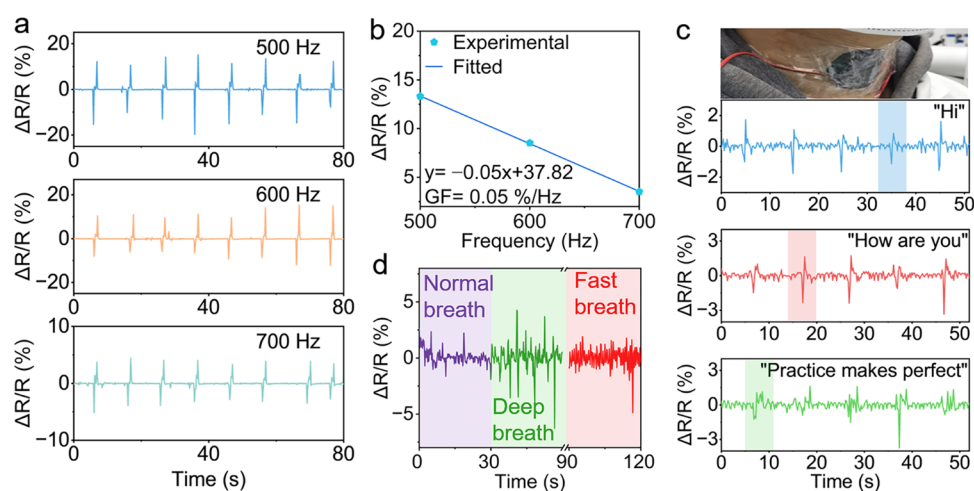
Figure 3. Vibration sensing performances and responses of the PAM−PVA−SA−rGO/NFs to human speaking and breathing. The relative resistance changes in responses to the vibrations of different frequencies (a, b) and human speaking (c) and breathing (d) movements of the throat. The photo (top of c) was the actual test in responses to human speaking and breathing. The size of each PAM−PVA−SA−rGO/NF was 5 cm diameter (a−d).

(R_t) of the basic conductive unit could be described as the following equation

$$R_t = \frac{R_1 + R_2 + 2R_C}{2} \tag{2}$$

where R_1 and R_2 are the resistances of the warp and weft yarns in the basic conductive unit without applied strain, respectively. And R_C is the contact resistance without applied strain. The contact resistance could be expressed by Holm's contact theory[32]

$$R_C = \frac{\rho}{2}\sqrt{\frac{\pi H}{nP}} \tag{3}$$

where ρ, H, n, and P represent the resistivity, the hardness, the number of contact points, and the contact pressure, respectively. R_C increased with a decreasing number of contact points (n), assuming that the constant resistivity and hardness remain unchanged. Therefore, $\Delta R/R$ increased with the increasing tensile strain.

Based on the strain sensing performances, the PAM−PVA−SA−rGO/NFs can be applied to intelligent sleeves to monitor human motions (Figure 2f). The resistance changes can be observed during elbow bending and twisting of a volunteer wearing the intelligent sleeves (Figures 2g,h and S4), as demonstrated in Movie S1. This was attributed to the mechanical stretching of the hydrogels within the intelligent sleeves, leading to a corresponding increase in resistance. Notably, the relative resistance signals were observed to remain regular and stable during continuous bending and twisting, indicating a high degree of responsiveness to partial human movements. Besides, considering the loss of water during use, the PAM−PVA−SA−rGO/NFs would be simply packaged in applications. And according to the analysis of the loss of weight (Figure S8), the simply packaged PAM−PVA−SA−rGO/NFs could meet the needs of applications. Therefore, the above results suggested that the strain-sensitive PAM−PVA−SA−rGO/NFs presented promising potential toward the development of advanced wearable technologies.

Furthermore, the pressure sensing performances of the PAM−PVA−SA−rGO/NFs are explored in Figure S5. The PAM−PVA−SA−rGO/NFs showed the corresponding elec-

trical signals under pressures of 1−4 N. Notably, $\Delta R/R$ slowly increased under the pressures of 1−3 N and then rapidly increased under the pressures of 3−4 N. The $\Delta R/R$ values to pressures were linearly fitted by the equations $y = 0.03x + 0.13$ and $y = 0.26x − 0.57$, respectively, and the calculated GF values were 0.03 and 0.26%/N in the ranges of 1−3 and 3−4 N, respectively. The pressure applied on the PAM−PVA−SA−rGO/NFs caused the slipping among rGO layers in the PAM−PVA−SA−rGO system, and thus the conductive pathways reduced, leading to a slow increase in $\Delta R/R$ under the pressures of 1−3 N.[33] As the pressures further increased, the conductive pathways were further broken due to the generation of cracks, leading to a significant decrease in the number of conductive pathways, hindering electron transfer, and thus, the $\Delta R/R$ increased rapidly.[34,35]

Subsequently, to explore the vibration sensing performances and applications of the PAM−PVA−SA−rGO/NFs, the $\Delta R/R$ values in responses to different vibration frequencies were measured. The PAM−PVA−SA−rGO/NFs exhibited the corresponding electrical signals with vibration frequencies from 500 to 700 Hz (Figure 3a,b). The resistance signals implied the stability and accuracy in detection of vibrations at specific frequencies. With the frequencies increased from 500 to 700 Hz, $\Delta R/R$ decreased. The reason might be that the higher vibration caused the knitted structures compounded with the conductive materials in the PAM−PVA−SA−rGO/NFs to have more electrical contact, leading to an increase in the number of conductive pathways, and therefore, the $\Delta R/R$ decreased. $\Delta R/R$ to frequency was linearly fitted by the equation $y = −0.05x + 37.82$, and it was concluded that the GF of the vibration in the range of 500−700 Hz was about 0.05%/Hz, as shown in Figure 3b. The excellent linearity held immense potential for practical applications of the PAM−PVA−SA−rGO/NFs.

Based on these vibration sensing performances, the PAM−PVA−SA−rGO/NFs could be applied to monitor practical activities in real time when connected to the human throat, such as tracking human speech and respiration. Figure 3c,d recorded the corresponding resistance responses when a piece of 5 cm diameter PAM−PVA−SA−rGO/NF with a simple package was attached to the human throat, by which human
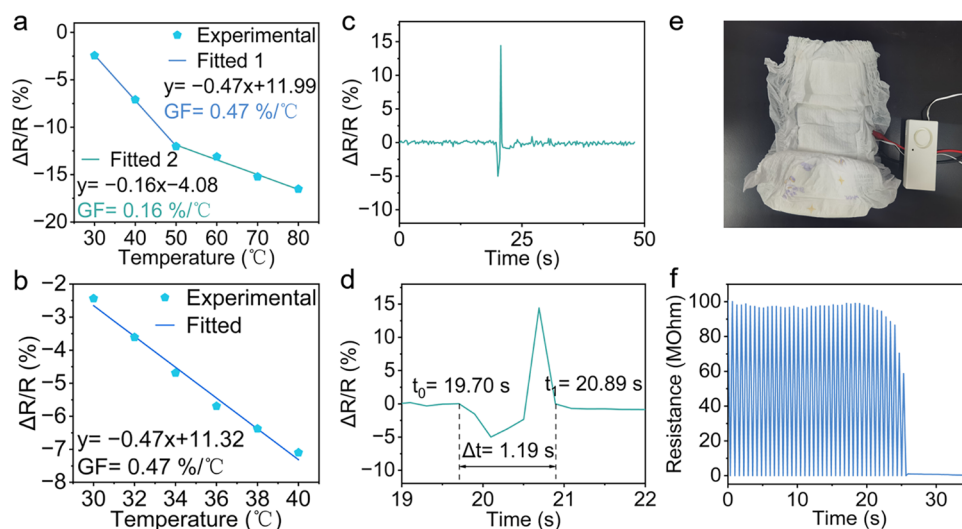
Figure 4. Temperature sensing performances of the PAM−PVA−SA−rGO/NFs and application in intelligent diaper alarms. The relative changes of the resistance with different temperatures of 30−80 °C (a) and those of 30−40 °C (b). (c) Relative changes of the resistance with urine of 0.2 mL. (d) Partial enlarged graph of (c) in 19−22 s to describe the time accuracy of urine presence detection of the PAM−PVA−SA−rGO/NFs. (e) Photo of the actual test of an intelligent diaper alarm based on the PAM−PVA−SA−rGO/NFs. (f) Resistance changes of the intelligent diaper alarm.

speaking and breathing movements of the throat were tracked. The output waveforms were stable and repeatable when a volunteer spoke the sentences "*Hi*", "*How are you*", and "*Practice makes perfect*", as depicted in Figure 3c. When the throat repeated the same sentence, there was a regular waveform. And the resistance waveforms grew more complex as the sentences became longer. This might be attributed to the fact that the vocal cord vibrated when the human was speaking, and the resulting vibrations were more complex with longer sentences uttered, leading to the more complex resistance change waveforms due to the sensitivity of the PAM−PVA−SA−rGO/NFs to vibrations.

As another application of vibration sensing performance, the respiration monitoring of the PAM−PVA−SA−rGO/NFs was further investigated. Figure 3d reveals that the PAM−PVA−SA−rGO/NFs could monitor real-time electrical signals under normal breathing, deep breathing, and fast breathing. These varying respiratory states differed in frequency and intensity. And thus, the waveforms were significantly different when a volunteer was under normal breathing, deep breathing, and fast breathing with a piece of 5 cm diameter PAM−PVA−SA−rGO/NF attached to the throat. In particular, the frequency of fast breathing was higher than that of normal breathing and deep breathing, while the intensity of deep breathing was the highest. Therefore, the above results illustrated the potential utility of the PAM−PVA−SA−rGO/NFs in recognizing and monitoring human speaking and breathing movements based on their good vibration sensing performances.

Additionally, the temperature sensing performances of the PAM−PVA−SA−rGO/NFs were evaluated as shown in Figure 4a,b. The PAM−PVA−SA−rGO/NFs showed the corresponding electrical signals in the temperature range 30−80 °C at a gradient of 10 °C, as depicted in Figure 4a. Both in the temperature ranges of 30−50 and 50−80 °C, the $\Delta R/R$ values to temperatures demonstrated linear changes, and the fitted linear equations were $y = -0.47x + 11.99$ and $y = -0.16x - 4.08$, respectively. Consequently, the calculated GF values were 0.47 and 0.16%/°C in the ranges of 30−50 and 50−80 °C, respectively. The resistances of the PAM−PVA−SA−rGO/

NFs decreased with the temperatures increasing, meaning that the PAM−PVA−SA−rGO/NFs exhibited a negative temperature coefficient (NTC) behavior, and this would be due to the NTC properties of rGO. The resistance at a certain temperature (T) could be expressed as the following equation[36]

$$R(T) = R(T_0) - \left(\frac{\hbar}{e^2}\right)\left(\frac{4TV_0}{\hbar\nu^2 E_f \tau_0}\right) \tag{4}$$

where $R(T)$ and $R(T_0)$ represent the resistance at the temperature of T and T_0, respectively. And then, $\hbar$, e, ν, E_f, τ_0, and V_0 mean the Planck constant, the electron charge, the velocity, the Fermi energy, the backscattering rate of the atomic sharp defects in the lattice, and the characteristic interaction constant, respectively. As the temperatures increased from 30 to 80 °C, the $\Delta R/R$ values decreased, which might be attributed to the following two reasons: (i) the increasing probability of electron transition under the action of thermal activation and (ii) the enhancement of tunneling and hopping transports among the rGO.[37] After 50 °C, the resistance changes slowed, possibly due to the effect of high temperature on the interaction within the PAM−PVA−SA−rGO system. Additionally, in situ heating Raman spectroscopy from 30 to 80 °C was also conducted to investigate the functional group/chemical bond changing during the heat stimuli (Figure S9), and its results consistent with the above further confirmed these mechanisms.

Further exploration into the temperature range of 30−40 °C, which was close to body temperature, was carried out in light of the higher GF and better sensitivity observed in the range of 30−50 °C. As depicted in Figure 4b, the $\Delta R/R$ values changed when the temperatures ranged from 30 to 40 °C with intervals of 2 °C, indicating that the distinguishability of the thermal responses was estimated to be 2 °C. When the temperatures ranged from 30 to 40 °C, $\Delta R/R$ to temperature showed a good linear response, with a fitted linear equation of $y = -0.47x + 11.32$ and the corresponding GF value of 0.47%/°C, consistent with the GF value observed in the range of 30−

50 °C. These results demonstrated the great potential of the PAM−PVA−SA−rGO/NFs in monitoring body temperature.

Therefore, the PAM−PVA−SA−rGO/NFs could be utilized for the purpose of detecting urine presence, which was typically at a temperature of 37 °C, closely resembling body temperature. Urea and NaCl were the most typical solutes in infant urine. The content of urea was about 1.5% and that of NaCl was 1.1%. To simulate infant urine for the urine presence detection experiment, a 37 °C urea/NaCl mixed solution was prepared with the corresponding concentrations. The experimental setup involved the addition of the prepared urine solution onto the surface of a piece of 5 cm diameter PAM−PVA−SA−rGO/NF, with an area of 78.5 cm^2. The observed results revealed that a minimum of 0.2 mL of urine was required to induce a significant change in the output value of the resistance (Figure 4c). In other words, the urine presence detecting threshold (DT) of the PAM−PVA−SA−rGO/NF was 0.2 mL, and at this time, the DT of the unit area (DTUA) was 2.55×10^{-3} mL cm^{-2}. As demonstrated in Figure 4d, t_0 represents the time at which 0.2 mL of urine contacted the PAM−PVA−SA−rGO/NF surface, and the urine presence detection exhibited a time accuracy (TA) of 1.19 s, which meant that the detection could be completed in about 1 s without obvious hysteresis. The response time of the detection was tolerable compared with the human reaction time, and therefore, it held significant promise for use in the application of real-time detection. In addition, utilizing the aforementioned features, the PAM−PVA−SA−rGO/NFs could be applied to intelligent diaper alarms to detect human motions (Figure 4e). In an intelligent diaper alarm, the PAM−PVA−SA−rGO/NF was connected to an alarm and the alarm was resistance-responsive and had no response to pressure and temperature. As displayed in Movie S2 and Figure 4f, it demonstrated the response of an intelligent diaper alarm upon the addition of a urine solution to the diaper. It could be observed that when the urine solution added to the diaper reached a certain value, significant changes in the output resistance of the intelligent diaper alarm were detected, and the output resistance was maintained at a relatively low value due to the conductivity of urine. Upon monitoring these changes, the diaper alarm would produce an audible alarm signal. Therefore, the above results revealed that the intelligent diaper alarms could effectively monitor human partial behaviors in real-time and generate detectable auditory signals, which further highlighted the tremendous potential of the PAM−PVA−SA−rGO/NFs for intelligence systems, feedback devices, and wearable devices.

3. CONCLUSIONS

In summary, we designed multistimuli responsive PAM−PVA−SA−rGO/NFs fabricated with NFs and a PAM−PVA−SA−rGO quaternary system using a one-step free radical polymerization method with ultrasonic dispersion. In the PAM−PVA−SA−rGO quaternary system, PAM−PVA−SA formed a triple interpenetrating network hydrogel, and rGO was incorporated as a conductive filler. The PAM−PVA−SA−rGO quaternary system improved the mechanical properties of the PAM−PVA−SA−rGO/NFs due to the triple inter-penetrating network structure and synergized interactions between rGO and PAM, PVA, and SA chains. Furthermore, the PAM−PVA−SA−rGO/NFs demonstrated good wettabil-ity and showed promising performance in strain, pressure, vibration, and temperature sensing. Based on these perform-ances, the PAM−PVA−SA−rGO/NFs could be applied in

multiapplication scenarios, such as intelligent sleeves and diaper alarms, and monitoring human speaking and breathing. These results indicated that the PAM−PVA−SA−rGO/NFs would have significant implications for the future development of intelligence systems, soft robotics, wearable devices, etc.

4. METHODS

4.1. Synthesis of Materials. Raw materials comprise acrylamide (Am), sodium alginate (SA), poly(vinyl alcohol) (PVA), graphene oxide (GO), N,N′-methylenebis(acrylamide) (Bis), ammonium persulfate (APS), N,N,N′,N′-tetraethylethylenediamine (TEMED), hydrazine hydrate, and deionized water. All reagents were purchased from Aladdin Chemical Co., Ltd. First, hydrazine hydrate was added into the GO suspension (reduction of 3 mL of GO suspension with 1 μL of hydrazine hydrate), and the reaction was performed in an oil bath at 80 °C for 12 h. And the product was separated and dried to obtain rGO. Second, PVA and SA were dissolved in deionized water, respectively, to obtain the concentrations of 2.4 and 1 wt %, respectively, with vigorous stirring for 2 h at 90 °C. Then, 2.8 M Am, 0.0025 M Bis, 0.0008 M APS, and 0.0094 M TEMED and rGO were ultrasonically dispersed in 10 mL of PVA and SA mixed solution. Finally, the fabrics were dipped into the mixture. The PAM−PVA−SA−rGO/NFs can be obtained by free radical polymerization.

4.2. Characterization of Morphology and Components. The morphologies of the samples were obtained using a scanning electron microscope (SEM) at 5.0 kV. The water contact angle (WCA) was measured using a JY-82C contact angle meter. During the WCA test, 16 μL of water was carefully dropped onto the samples. Fourier transform infrared (FTIR) spectroscopy measurements were recorded with a Thermo Scientific Nicolet iS20. In situ heating Raman spectroscopy measurements used a Horiba LaRAM HR Evolution with a laser wavelength of 633 nm. The heating rate was 5 °C·min^{-1}. After being kept at the target temperature for 5 min, the sample was performed for constant-temperature Raman spectroscopy measure-ments.

4.3. Measurement of Electrical Signals. Electrochemical impedance spectroscopy (EIS) was obtained with an electrochemical workstation (CHI660E) at room temperature. The ionic conductivity was calculated according to the equation: $\sigma = \frac{L}{R_b \cdot S}$, where σ, L, R_b, and S represent the ionic conductivity of the sample, thickness of the sample, bulk resistance of the sample, and electrode contacting area, respectively. The other electrical signals were measured with a Keithley 2400 SourceMeter.

4.4. Mechanical Property Measurement. The samples with a size of 2 cm × 4 cm were tensed 1 cm along the long side, and the force values were recorded by a Suce SH-III digital push-60 pull meter. During rubbing and sticking with tape, a self-designed sticky hydrogel was designed and prepared for use as the tape. The tensile stress−strain behaviors of the prepared hydrogels were determined on an electronic universal testing machine (INSTRON 3367). The tensile tests were investigated at 25 °C and the testing speed was 5 mm min^{-1}.

4.5. Rheological Property Measurement. The rheological properties of hydrogel samples were evaluated by a rheometer (Thermo HAAKE MARS 60, Germany) with a 20 mm parallel plate. Under the condition of a frequency of 1 Hz, the dynamic strain sweep spectra of the hydrogels were obtained in the strain range mode (0.1−1000 Pa) to determine the linear viscoelastic regime.

4.6. Fabrication of the Intelligent Sleeves. The PAM−PVA−SA−rGO/NFs with a size of 12 cm × 15 cm were sewn to the elbows of the sleeves by using needle and thread to obtain the intelligent sleeves.

4.7. Testing of the Intelligent Diaper Alarms. The prepared urine solution simulated infant urine with 1.5% urea and 1.1% NaCl at a temperature of 37 °C. The PAM−PVA−SA−rGO/NF sample was placed in the diaper and connected to an alarm, which was self-designed resistance-responsive and had no response to pressure and

temperature. The prepared urine solution was added to the diaper surface during testing.

■ ASSOCIATED CONTENT

Data Availability Statement

The data that has been used is confidential.

ⓢ Supporting Information

The Supporting Information is available free of charge at https://pubs.acs.org/doi/10.1021/acsapm.3c00957.

Movie S1: Movie showing the resistance changes during elbow bending and twisting of a volunteer wearing the intelligent sleeves (AVI)

Movie S2: Movie showing the responses of an intelligent diaper alarm upon the addition of urine solution to the diaper (AVI)

Additional experimental details and properties of PAM−PVA−SA−rGO/NFs, including electrochemical impedance spectroscopy, water contact angle, the SEM image, FTIR spectra, and digital photos of tensile testing; resistance−time relationships with bending and twisting movements; pressure sensing performances; rheological properties; tensile stress−strain curve; change of weight; and in situ Raman spectra (PDF)

■ AUTHOR INFORMATION

Corresponding Authors

Hanqing Dai − *Academy for Engineering and Technology, Fudan University, Shanghai 200433, China;* ⓞ orcid.org/0000-0001-5383-8702; Email: 98dhq@sina.com

Ruiqian Guo − *Institute for Electric Light Sources, School of Information Science and Technology, Fudan University, Shanghai 200433, China; Academy for Engineering and Technology, Fudan University, Shanghai 200433, China;* ⓞ orcid.org/0000-0002-0498-0363; Email: rqguo@fudan.edu.cn

Guoqi Zhang − *Department of Microelectronics, Delft University of Technology, Delft 2628 CD, Netherlands;* Email: G.Q.Zhang@tudelft.nl

Wanlu Zhang − *Institute for Electric Light Sources, School of Information Science and Technology, Fudan University, Shanghai 200433, China;* Email: fdwlzhang@fudan.edu.cn

Wei Wei − *College of Electronic and Optical Engineering, Nanjing University of Posts and Telecommunications, Nanjing 210023, China;* Email: weiwei@njupt.edu.cn

Authors

Yuanyuan Chen − *Institute for Electric Light Sources, School of Information Science and Technology, Fudan University, Shanghai 200433, China*

Yukun Yan − *Institute for Electric Light Sources, School of Information Science and Technology, Fudan University, Shanghai 200433, China*

Zhiyan Piao − *Institute for Electric Light Sources, School of Information Science and Technology, Fudan University, Shanghai 200433, China*

Hanxu Lu − *Institute for Electric Light Sources, School of Information Science and Technology, Fudan University, Shanghai 200433, China*

Zhe Hu − *Institute for Electric Light Sources, School of Information Science and Technology, Fudan University, Shanghai 200433, China*

Complete contact information is available at:

https://pubs.acs.org/10.1021/acsapm.3c00957

Author Contributions

H.Q.D. and Y.Y.C. conceived the project and designed the experiments. Y.Y.C. performed all data collection. Y.Y.C. and H.Q.D. conducted the analysis of experimental data. Y.Y.C. wrote the manuscript. H.Q.D., W.L.Z., G.Q.Z., W.W., and R.Q.G. corrected the manuscript. Others carried out auxiliary work related to these experiments.

Notes

The authors declare no competing financial interest.

■ ACKNOWLEDGMENTS

■ REFERENCES

(1) Lee, J.; Zambrano, B. L.; Woo, J.; Yoon, K.; Lee, T. Recent advances in 1D stretchable electrodes and devices for textile and wearable electronics: materials, fabrications, and applications. *Adv. Mater.* **2020**, *32*, No. 1902532.

(2) Liu, Z.; Li, H.; Shi, B.; Fan, Y.; Wang, Z. L.; Li, Z. Wearable and implantable triboelectric nanogenerators. *Adv. Funct. Mater.* **2019**, *29*, No. 1808820.

(3) Lin, M. Y.; Hu, H. J.; Zhou, S.; Sheng, X. Soft wearable devices for deep-tissue sensing. *Nat. Rev. Mater.* **2022**, *7*, 850.

(4) Song, D.; Zeng, M. J.; Peng, M.; Jia, X.; Gao, F. L.; Yu, Z.; Li, X. F. Electrically conductive and highly compressible anisotropic MXene-wood sponges for multifunctional and integrated wearable devices. *J. Mater. Sci. Technol.* **2023**, *144*, 102.

(5) Liu, H.; Yu, L.; Zhao, B.; Ni, Y.; Gu, P.; Qiu, H.; Zhang, W.; Chen, K. Bio-inspired color-changing and self-healing hybrid hydrogels for wearable sensors and adaptive camouflage. *J. Mater. Chem. C* **2022**, *11*, 285.

(6) Tan, C.; Dong, Z.; Li, Y.; Zhao, H.; Huang, X.; Zhou, Z.; Jiang, J. W.; Long, Y. Z.; Jiang, P.; Zhang, T. Y.; Sun, B. A high performance wearable strain sensor with advanced thermal management for motion monitoring. *Nat. Commun.* **2020**, *11*, No. 3530.

(7) Fan, W.; He, Q.; Meng, K.; Tan, X.; Zhou, Z.; Zhang, G.; Yang, J.; Wang, Z. L. Machine-knitted washable sensor array textile for precise epidermal physiological signal monitoring. *Sci. Adv.* **2020**, *6*, eaay2840.

(8) Wang, J. L.; Lu, C. H.; Zhang, K. Textile-based strain sensor for human motion detection. *Energy Environ. Mater.* **2020**, *3*, 80.

(9) Ates, H. C.; Yetisen, A. K.; Güder, F.; Dincer, C. Wearable devices for the detection of COVID-19. *Nat. Electron.* **2021**, *4*, 13.

(10) He, F.; You, X.; Gong, H.; Yang, Y.; Bai, T.; Wang, W.; Guo, W.; Liu, X.; Ye, M. Stretchable, biocompatible, and multifunctional silk fibroin-based hydrogels toward wearable strain/pressure sensors and triboelectric nanogenerators. *ACS Appl. Mater. Interfaces* **2020**, *12*, 6442.

(11) Nyein, H. Y. Y.; Bariya, M.; Tran, B.; Ahn, C. H.; Brown, B. J.; Ji, W.; Davis, N.; Javey, A. A wearable patch for continuous analysis of thermoregulatory sweat at rest. *Nat. Commun.* **2021**, *12*, No. 1823.

(12) Wang, R.; Du, Z.; Xia, Z.; Liu, J.; Li, P.; Wu, Z.; Yue, Y.; Xiang, Y.; Meng, J.; Liu, D.; Xu, W.; Tao, X.; Tao, G.; Su, B. Magnetoelectrical clothing generator for high-performance transduction from biomechanical energy to electricity. *Adv. Funct. Mater.* **2022**, *32*, 21076.

(13) Li, H.; Zhou, S. Y.; Du, X. Y.; Wang, J. N.; Cao, R.; Xing, Y.; Li, C. A compound yarn based wearable triboelectric nanogenerator for

self-powered wearable electronics. *Adv. Mater. Technol.* **2018**, *3*, No. 1800065.

(14) Dong, S.; Xu, F.; Sheng, Y.; Guo, Z.; Pu, X.; Liu, Y. Seamlessly knitted stretchable comfortable textile triboelectric nanogenerators for E-textile power sources. *Nano Energy* **2020**, *78*, No. 105327.

(15) He, T.; Shi, Q.; Wang, H.; Wen, F.; Chen, T.; Ouyang, J.; Lee, C. Beyond energy harvesting-multi-functional triboelectric nanosensors on a textile. *Nano Energy* **2019**, *57*, 338.

(16) Bai, Z.; Wang, X.; Huang, M.; Zheng, M.; Yue, O.; Hao, D.; Wang, Y.; Zou, X.; Cui, B.; Xie, L.; Zha, S.; Ju, H.; Liu, X. Versatile nano-micro collagen fiber-based wearable electronics for health monitoring and thermal management. *J. Mater. Chem. A* **2023**, *11*, 726.

(17) Yang, Y.; Sun, N.; Wen, Z.; Cheng, P.; Zheng, H.; Shao, H.; Xia, Y.; Chen, C.; Lan, H.; Xie, X.; Zhou, C.; Zhong, J.; Sun, X.; Lee, S. T. Liquid-metal-based super-stretchable and structure-designable triboelectric nanogenerator for wearable electronics. *ACS Nano* **2018**, *12*, 2027.

(18) Hu, S.; Han, J.; Shi, Z.; Chen, K.; Xu, N.; Wang, Y.; Zheng, R.; Tao, Y.; Sun, Q.; Wang, Z. L.; Yang, G. Biodegradable, super-strong, and conductive cellulose macrofibers for fabric-based triboelectric nanogenerator. *Nano-Micro Lett.* **2022**, *14*, 115.

(19) Xu, R.; Qu, L.; Tian, M. Touch-sensing fabric encapsulated with hydrogel for human-computer interaction. *Soft Matter* **2021**, *17*, 9014.

(20) Fu, Q.; Liu, Y.; Liu, T.; Mo, J.; Zhang, W.; Zhang, S.; Luo, B.; Wang, J.; Qin, Y.; Wang, S.; Nie, S. Air-permeable cellulosic triboelectric materials for self-powered healthcare products. *Nano Energy* **2022**, *102*, No. 107739.

(21) Sun, Q.; Wang, L.; Ren, G.; Zhang, L.; Sheng, H.; Zhu, Y.; Wang, H.; Lu, G.; Yu, H. D.; Huang, W. Smart band-aid: multifunctional and wearable electronic device for self-powered motion monitoring and human-machine interaction. *Nano Energy* **2022**, *92*, No. 106840.

(22) Xie, Z.; Chen, Z.; Hu, X.; Mi, H. Y.; Zou, J.; Li, H.; Liu, Y.; Zhang, Z.; Shang, Y.; Jing, X. Ultrastretchable, self-healable and adhesive composite organohydrogels with a fast response for human-machine interface applications. *J. Mater. Chem. C* **2022**, *10*, 8266.

(23) El-Sayed, N. S.; Kiey, S. A. A.; Darwish, A.; Turky, G.; Kamel, S. High performance hydrogel electrodes based on sodium alginate-g-poly (AM-co-ECA-co-AMPS) for supercapacitor application. *Int. J. Biol. Macromol.* **2022**, *218*, 420.

(24) Chu, J. H.; Tong, L. B.; Zhang, J. B.; Kamado, S.; Jiang, Z. H.; Zhang, H. J.; Sun, G. X. Bio-inspired graphene-based coatings on Mg alloy surfaces and their integrations of anti-corrosive/wearable performances. *Carbon* **2019**, *141*, 154.

(25) Peng, Y.; Zhao, X. Z.; Liu, C. K. Directional solution transfer of a 3D solar evaporator inhibiting salt crystallization. *J. Mater. Chem. A* **2021**, *9*, 22472.

(26) Zhang, J.; Zhao, X.; Wang, Z.; Liu, Z.; Yao, S.; Li, L. Antibacterial, antifreezing, stretchable, and self-healing organohydrogel electrode based triboelectric nanogenerator for self-powered biomechanical sensing. *Adv. Mater. Interfaces* **2022**, *9*, No. 2200290.

(27) Wang, Y.; Lu, Y.; Zhang, J.; Hu, X.; Yang, Z.; Guo, Y.; Wang, Y. A synergistic antibacterial effect between terbium ions and reduced graphene oxide in a poly (vinyl alcohol)-alginate hydrogel for treating infected chronic wounds. *J. Mater. Chem. B* **2019**, *7*, 538.

(28) Zhang, L.; Jiang, Q.; Zhao, Y.; Yuan, J.; Zha, X.; Xie, H.; Kong, F.; Xiong, X. Strong and tough PAm/SA hydrogel with highly strain sensitivity. *J. Renewable Mater.* **2022**, *10*, 415.

(29) Li, Y.; Huang, L.; Tai, G.; Yan, F.; Cai, L.; Xin, C.; Islam, S. A. Graphene oxide-loaded magnetic nanoparticles within 3D hydrogel form high-performance scaffolds for bone regeneration and tumour treatment. *Composites, Part A* **2022**, *152*, No. 106672.

(30) Ren, J.; Wang, X.; Zhang, A.; Zhang, L.; Zhao, L.; Li, Y.; Yang, W. Fabrication tough and electrically conductive graphene-based nanocomposite gels with self-oscillating performance. *Macromol. Res.* **2020**, *28*, 1253.

(31) Zhao, W.; Zheng, Y.; Qian, J.; Zhang, Z.; Jin, Z.; Qiu, H.; Zhu, C.; Hong, X. AgNWs/MXene derived multifunctional knitted fabric capable of high electrothermal conversion efficiency, large strain and temperature sensing, and EMI shielding. *J. Alloys Compd.* **2022**, *923*, No. 166471.

(32) Seyedin, S.; Razal, J. M.; Innis, P. C.; Jeiranikhameneh, A.; Beirne, S.; Wallace, G. G. Knitted strain sensor textiles of highly conductive all-polymeric fibers. *ACS Appl. Mater. Interfaces* **2015**, *7*, 21150.

(33) Zhang, W.; Yin, B.; Wang, J.; Mohamed, A.; Jia, H. Ultrasensitive and wearable strain sensors based on natural rubber/graphene foam. *J. Alloys Compd.* **2019**, *785*, 1001.

(34) Wu, Y.-h.; Liu, H.; Chen, S.; Dong, X.; Wang, P.; Liu, S.; Lin, Y.; Wei, Y.; Liu, L. Channel crack-designed gold@PU sponge for highly elastic piezoresistive sensor with excellent detectability. *ACS Appl. Mater. Interfaces* **2017**, *9*, 20098.

(35) Zheng, Q.; Lee, J.; Shen, X.; Chen, X.; Kim, J. K. Graphene-based wearable piezoresistive physical sensors. *Mater. Today.* **2020**, *36*, 158.

(36) Huang, L.; Zeng, Y.; Liu, X.; Tang, D. Pressure-based immunoassays with versatile electronic sensors for carcinoembryonic antigen detection. *ACS Appl. Mater. Interfaces* **2021**, *13*, 46440.

(37) Trung, T. Q.; Le, H. S.; Dang, T. M. L.; Ju, S.; Park, S. Y.; Lee, N. E. Freestanding, fiber-based, wearable temperature sensor with tunable thermal index for healthcare monitoring. *Adv. Healthcare Mater.* **2018**, *7*, No. 1800074.